Erik Jonsson School of Engineering and Computer Science

2012-10-22

Fundamental Limitations of Hot-Carrier Solar Cells

A.P. Kirk and M. V. Frischetti

Fundamental limitations of hot-carrier solar cells

A. P. Kirk[*] and M. V. Fischetti[†]

University of Texas at Dallas, Department of Materials Science and Engineering, Richardson, Texas 75080, USA

Sunlight-generated hot-carrier transport in strongly absorbing direct band-gap GaAs—among the most optimal of semiconductors for high-efficiency solar cells—is simulated with an accurate full-band structure self-consistent Monte Carlo method, including short- and long-range Coulomb interaction, impact ionization, and optical and acoustic phonon scattering. We consider an ultrapure 100-nm-thick intrinsic GaAs absorber layer designed with quasiballistic carrier transport that achieves complete photon absorption down to the band edge by application of careful light trapping and that has a generous hot-carrier retention time of 10 ps prior to the onset of carrier relaxation. We find that hot-carrier solar cells can be severely limited in performance due to the substantially reduced current density caused by insufficient extraction of the widely distributed hot electrons (holes) through the requisite energy selective contacts.

PACS number(s): 88.40.hj

I. INTRODUCTION

When a photon with energy $\hbar\omega \geqslant E_g$ is first absorbed by a semiconductor (with energy band gap E_g), the immediate aftermath is the photogeneration of an electron-hole pair. The term *hot carrier* refers to the fact that prior to any scattering with lattice phonons, a photoexcited electron (hole) with energy $\hbar\omega > E_g$ has energy in excess of the band gap and thus is considered to be "*hot*". After multiple scattering events with phonons, the hot electron (hole) gives up its excess energy as heat by relaxing to the fundamental conduction (valence) band edge. This process represents waste in the context of a solar cell. For example, considering a single *p–n* junction Si solar cell ($E_g = 1.12$ eV) with a detailed balance-limiting power conversion efficiency of 33.4% under the standard ASTM G173-03 global air mass 1.5 (AM1.5G) solar spectrum[1] at 298 K, relaxation losses are substantial at 47.4% (with the remaining 19.2% from the lack of absorption of sub-band-gap photons). Therefore, in the spirit of finding ways to reduce this substantial relaxation loss component, the concept of a hot-carrier solar cell (HCSC) emerges.

HCSCs are a class of solar photovoltaic energy conversion device proposed in 1982 by Ross and Nozik[2] that aim to collect and do work from photogenerated hot carriers[3] prior to relaxation to the band edges. To avoid relaxation, carrier interaction (scattering) with phonons should be suppressed. There has been some discussion that a phonon bottleneck effect could help to temporarily suppress carrier relaxation by potentially reheating the hot-electron gas.[4] Recently, however, from simulation of hot carriers in GaAs quantum wells under concentrated sunlight, it appears that hot phonons may not add any meaningful benefit,[5] while the use of confined structures (e.g., quantum dot arrays and superlattices) faces the opposite requirement of achieving strong confinement—required to minimize the density of final electron and phonon states available (phonon bottleneck) for unwanted dissipative collisions—while allowing efficient generation and collection of the carriers. Moreover, so far none of the attempts to fabricate HCSC, including those designs with nanostructures and hot phonons, has yielded notable performance despite the promise of efficiency exceeding[6] conventional solar cells that operate with relaxed charge carriers.

II. ENERGY SELECTIVE CONTACTS

In order to collect the hot carriers, it becomes necessary to use energy selective contacts (ESC) to allow for isentropic extraction of the hot carriers prior to relaxation. Suggested ESC architectures include quantum dot or atomic impurity structures[7] that for analytical purposes may be approximated by the common double-barrier resonant tunnel diode (RTD). Energy selectivity in this sense is defined by

$$\Delta E < k_B T, \tag{1}$$

where ΔE is the width of the resonant tunneling level, k_B is Boltzmann's constant, and T is the lattice temperature. A schematic outlining the basic elements of a HCSC is shown in Fig. 1.

III. HOT-CARRIER DISTRIBUTION

Due to the polychromatic nature of sunlight, the photogenerated hot electrons in a HCSC semiconductor will be widely distributed in the conduction bands as shown in Fig. 2.

The widely dispersed hot electrons would have to be redistributed into a well-ordered state such that (1) they would all occupy a discrete energy level corresponding to the hot-electron ESC and (2) have a tight momentum distribution directing them into the ESC—this alone would be important because quasiballistic transport would become necessary to deliver the hot electrons expeditiously to the discrete resonant tunneling level of the ESC prior to the onset of relaxation.

IV. RESONANT TUNNELING LEVEL

An ESC in the form of a RTD, meanwhile, is sensitive to the precise tunneling energy level. There is a sharp Lorentzian distribution[8] that underscores that an off-resonant condition leads to a dramatic decrease in peak tunneling current density.

By examining the tunneling transmission probability, $T(E)$, we can see this Lorentzian form

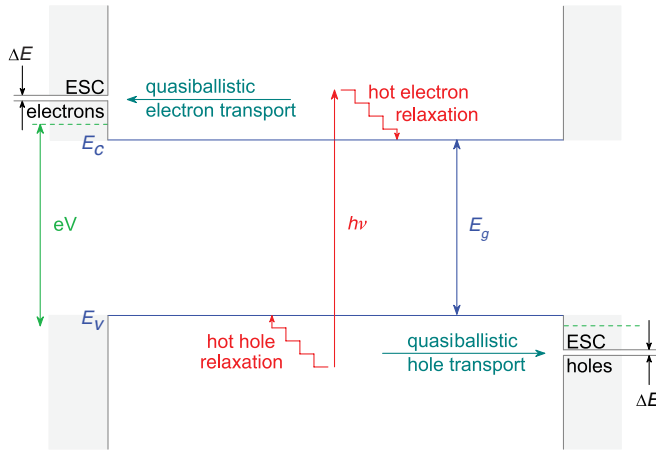$$T(E) \approx \frac{\Gamma_n^2/4}{\Gamma_n^2/4 + (E - E_n)^2}, \tag{2}$$

FIG. 1. (Color online) Schematic of a HCSC. Quasiballistic charge carrier transport must dominate and override charge carrier relaxation for proper HCSC operation. Hot electrons (holes) are extracted through the narrow ESC with width given by ΔE. Carriers that are not resonant with their respective ESC tunneling levels cannot be collected because they are repelled by the barriers represented by the shaded regions.

where Γ_n is the full width at half maximum (FWHM) of the discrete resonant energy level, E_n (and noting that E_n is the resonant tunneling level of our hot-electron ESC). In the case of a double-barrier RTD, Γ_n is given by

$$\Gamma_n = \sqrt{\frac{2\hbar^2 E_n T_1^2}{m^* b^2 R_1}}, \qquad (3)$$

where T_1 is the transmission coefficient of a single symmetric barrier, R_1 is the reflection coefficient of a single symmetric
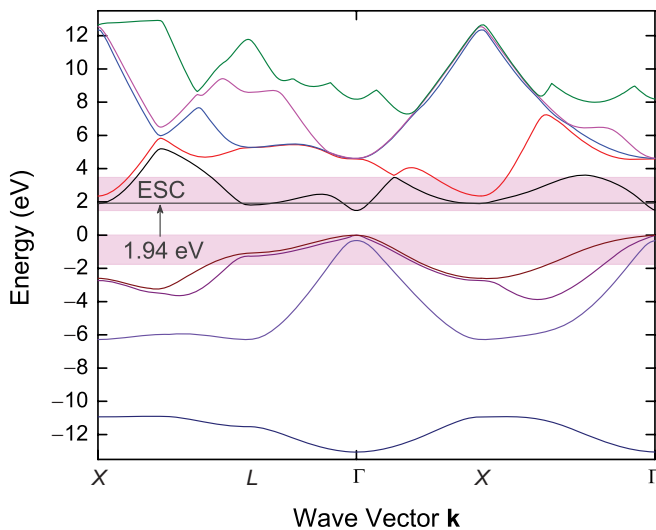

FIG. 2. (Color online) AM1.5G spectrum-generated hot-electron (hole) distribution shown in the upper (lower) shaded regions juxtaposed on a two-dimensional representation of the GaAs band structure, including a hot-electron ESC centered at 1.94 eV (horizontal line). The ESC has minimal, discrete interaction with the totality of conduction bands over which photogenerated hot electrons exist. Hot electrons above and below the ESC would have to be redistributed to it in order to be collected.

barrier, m^* is the electron effective mass, b is the width of the quantum well, and $\hbar$ is reduced Planck's constant. Therefore, any minor perturbation off of E_n (such as that caused by unavoidable interface roughness scattering) leads to a steep reduction in the peak tunneling current density on account of the reduced tunneling transmission probability.

V. HOT-CARRIER ENTROPY AND MOMENTUM

We know that ideal gases have entropy described by $S = k_B \log \Omega$, where Ω is the density of micro-states corresponding to the macro-state for which S is defined. The entropy of electrons (treated as an ideal gas to first order) in the conduction bands of a semiconductor may be expressed through the Sackur-Tetrode relationship (including Fermion spin) as

$$S = k_B N_e \left(\frac{5}{2} + \ln \frac{N_c}{n_e} \right), \qquad (4)$$

where N_e is the number of electrons, n_e is their concentration, and $N_c = 2(2\pi m^* k_B T / h^2)^{3/2}$ is the effective density of conduction band states.[9] Density of states will become an important topic later in this Article.

Furthermore, we know that just like the collision and scattering of gas molecules in a container, electrons in the conduction bands of a semiconductor also collide and scatter (e.g., with phonons or with each other)—consequently disorder (randomness) results. We will consider entropy, then, to be a measure of this disorder.[10] We know that it is improbable that hot electrons photogenerated as a result of absorption of polychromatic sunlight in a HCSC operating out in the field would be able to scatter (a disorderly process) into a well-behaved state such that they have a singular, discrete energy level required to ensure resonant tunneling at the discrete ESC.

In addition to the consideration of carrier energy, we can also take into consideration carrier momentum. Here, we may employ the integral path formalism of Boltzmann's transport equation developed by Chambers[11] and Budd,[12] which gives us a distribution function for scattered hot electrons

$$f(\mathbf{p}) = \int d\mathbf{p}' f(\mathbf{p}') K(\mathbf{p}', \mathbf{p});$$

$$K(\mathbf{p}', \mathbf{p}) = \int_0^\infty ds\, W(\mathbf{p}', \mathbf{p} - e\mathbf{F}s)$$

$$\times \exp\left[-\int_0^s ds'\, \tau^{-1}(\mathbf{p} - e\mathbf{F}s') \right], \qquad (5)$$

where $K(\mathbf{p}', \mathbf{p})$ is the scattering (collision) kernel, $\tau^{-1}(\mathbf{p}) = \int d\mathbf{p}' W(\mathbf{p}, \mathbf{p}')$, $\mathbf{p}$ is the momentum, $W(\mathbf{p}, \mathbf{p}')$ is the transition rate between $\mathbf{p}$ and $\mathbf{p}'$ as a result of collisions, e is the electronic charge, s is time, and $\mathbf{F}$ is the (uniform) electric field. We see that the hot electrons are described, again, as a distribution and thus cannot all be found with a singular fixed and uniform momentum.

In purely ideal electron-electron scattering, momentum is conserved but this does not imply that the direction of travel of the scattered electrons remains the same precollision versus postcollision. Conventional p–n junction solar cells are immune to randomization of carrier momentum because

the relaxed carriers diffuse (and drift) toward their respective electrodes. If the thickness of the absorber layer is designed to be less than the minority-carrier diffusion length, carriers may be effectively collected. In other words, in conventional solar cells operating under the drift-diffusion approximation, the Einstein relation given by $D = \mu(k_B T/e)$ is valid; this relation, however, is not valid for HCSC, where the temperature of the electrons is much greater than the lattice temperature.

As we cannot rely on diffusive charge carrier transport in HCSC, the hot electrons must undergo quasiballistic transport directly to the resonant tunneling level of the ESC as mentioned earlier. Therefore, revisiting Fig. 2 which, thematically, may be considered generic across semiconductors used for solar cells (e.g., Si, InP, GaAs) and once again thinking in terms of the distribution physics of electrons, we find all of these clues lead us to the fact that hot electrons cannot be redistributed to a singular energy level with a fixed and unified momentum vector. Importantly, at first order, the aforementioned semiconductors have, qualitatively speaking, quite similar electronic density of states (DoS), and therefore, we can only expect hot electrons to behave in a similar fashion. Even if we assume that the photogenerated hot electrons have become redistributed through impact ionization and Auger recombination together with electron-electron (and no electron-phonon) scattering to an equilibrium distribution at high temperature,[13] then Boltzmann's H theorem tells us that as the system approaches this hot equilibrium the entropy must increase.[10] Therefore, if entropy (disorder) increases, it would be counterintuitive to imagine that hot electrons would end up in an ordered state with a discrete energy and fixed momentum as this implies a reduction in entropy and an apparent violation of the H theorem.

VI. COMPUTATIONAL MODELING, INCLUDING MONTE CARLO SIMULATION

First used in 1966 by Kurosawa for modeling hot-carrier transport,[14] we also employ a Monte Carlo simulation program but in this case similar to a self-consistent ensemble Monte Carlo simulation plus Poisson solver developed by Fischetti and Laux at IBM,[15] with full (and accurate) band structure capability. To be clear, full-band Monte Carlo simulations were developed, in their own right, initially by Shichijo and Hess.[16] Below, we outline the basic aspects of our Monte Carlo simulation. We have neglected carrier-impurity scattering by operating under the assumption that our HCSC will be nominally undoped and of high crystal quality (e.g., grown under the conditions of an ultrahigh vacuum epitaxial growth technique such as molecular beam epitaxy).

A. Band structure

For our simulations we use the empirical nonlocal pseudopotential method following that of Chelikowsky and Cohen[17] to obtain an accurate and full band structure (conduction and valence bands) for GaAs, including spin-orbit splitting to optimally model the valence bands. We use the 0-K GaAs band structure (represented in standard two-dimensional format in Fig. 2) in our analysis and Monte Carlo carrier relaxation simulations rather than incorporate correction for

temperature (as a reminder, $E_{g,\text{GaAs}} = 1.42$ at 300 K). We expect the physics of hot-carrier scattering and distribution to be the same regardless of whether the 0- or 300-K GaAs band structure is used.

We now write down, using an expansion over Bloch waves, the Schrödinger-type equation in order to get the electron wave functions

$$\psi(\mathbf{r}) = \frac{1}{(N\Omega_c)^{1/2}} \sum_{\mathbf{k}} e^{i\mathbf{k}\cdot\mathbf{r}} \sum_{\mathbf{G}} u_{\mathbf{G}}(\mathbf{k})e^{i\mathbf{G}\cdot\mathbf{r}}, \qquad (6)$$

where Ω_c is the volume of the cell, $\mathbf{r}$ is location, $\mathbf{k}$ are the wave vectors, $\mathbf{G}$ are the reciprocal-lattice wave vectors, and $u_G(\mathbf{k})$ are the Bloch functions. We can then solve the following eigenvalue problem required to calculate the (GaAs) electronic bands from

$$\sum_{\mathbf{G}' < \mathbf{G}_{\text{max}}} H_{\mathbf{GG}'}(\mathbf{k})u_{\mathbf{G}'}(\mathbf{k}) = E(\mathbf{k})u_{\mathbf{G}}(\mathbf{k}), \qquad (7)$$

where we consider the cutoff, $\mathbf{G}_{\text{max}}$, noting that we only account for Bloch waves according to

$$\frac{\hbar^2}{2m}(\mathbf{k} + \mathbf{G})^2 \leqslant E_{\text{cutoff}}. \qquad (8)$$

Our Hamiltonian can be expressed as

$$\begin{aligned} H_{\mathbf{GG}'}(\mathbf{k}) = {}& \frac{\hbar^2}{2m}(\mathbf{k} + \mathbf{G})^2 + V_{\text{local}}(\mathbf{G} - \mathbf{G}') \\ & + \frac{8\pi}{\Omega_c}\sum_{l=0,2}\sum_{s=1,2} A_l^s(2l+1)P_l(\cos\theta_{\mathbf{KK}'}) \\ & \times S_s(\mathbf{G} - \mathbf{G}')F_l^s(\mathbf{K},\mathbf{K}') + H_{\mathbf{GG}'}^{\text{spin\_orbit}}(\mathbf{K},\mathbf{K}'), \quad (9) \end{aligned}$$

where the local form factors are given by

$$V_{\text{local}} = V_s\cos(\mathbf{G}\cdot\mathbf{t}) + iV_A\sin(\mathbf{G}\cdot\mathbf{t}), \qquad (10)$$

and V_S and V_A are the symmetric and antisymmetric form factors, respectively, whereas $\mathbf{t}$ is the vector $a/8 \times (1,1,1)$. Meanwhile, A_l^s is the energy dependent l-well depth for ion s, P_l are the Legendre polynomials, S_s is the atomic structure factor for ion s, F_l^s are the nonlocal well functions, and $\mathbf{K} = \mathbf{k} + \mathbf{G}$, while $\mathbf{K}' = \mathbf{k} + \mathbf{G}'$. The final term in Eq. (9) is the spin-orbit Hamiltonian, $H_{\mathbf{GG}'}^{\text{spin\_orbit}}(\mathbf{K},\mathbf{K}') = (\mathbf{K} \times \mathbf{K}') \cdot \sigma\{-i\lambda_S\cos[(\mathbf{G} - \mathbf{G}')\cdot\mathbf{t}] + \lambda_A\sin[(\mathbf{G} - \mathbf{G}')\cdot\mathbf{t}]\}$, where $\lambda_S = 1/2(\lambda_1 + \lambda_2)$, $\lambda_A = 1/2(\lambda_1 - \lambda_2)$, $\lambda_1 = \mu B_1(\mathbf{K})B_1(\mathbf{K}')$, $\lambda_2 = (\mu_2/\mu_1)B_2(\mathbf{K})B_2(\mathbf{K}')$, $B_n(\mathbf{K}) = \beta\int_0^\infty j_l(\mathbf{K}r)R(r)r^2 dr$, and σ are the Pauli spin states, μ is an empirical parameter, while $\mu_{1(2)}$ are the outermost p-type orbital spin-orbit energies, β is a normalization constant, j_l are the spherical Bessel functions, and R is the radial component of the core wave function.[17] For our simulations, we use empirical pseudopotential form factors from Fischetti,[18] which, in turn, represent minor modification from the original form factors given by Chelikowsky and Cohen.[17]

B. Interpolation

In our program, the band structure (the five lowest-lying conduction bands plus four highest-lying valence bands) and the hot-carrier scattering events are calculated in the first octant of the Brillouin zone (taking advantage of the inherent

symmetry of zinc-blende GaAs). We discretize the octant into a total of 5775 cubes (20 points along the Γ to X line) each of which has sides of dimension given by $D_k = 0.05 \times (2\pi/a)$ where a is the lattice constant of GaAs ($\sim$5.653 Å).[15] An electron (hole) in band n with wave vector $\mathbf{k}$ is mapped into the first octant. We store the sign transformations required to map a $\mathbf{k}$-point into this first octant because they will be used to allow us to then convert the group velocity back to the original point outside the first octant (i.e., taking into consideration the entire Brillouin zone). A direct interpolation process is used in order to integrate the equations of motion for carrier free flight. We briefly interrupt, here, to write down the aforementioned equations of motion for carrier free flight given by

$$\frac{d\mathbf{r}}{dt} = \frac{1}{\hbar}\nabla_{\mathbf{k}}E(\mathbf{k}), \tag{11}$$

$$\frac{d\mathbf{k}}{dt} = \frac{e}{\hbar}\nabla_{\mathbf{r}}\varphi(\mathbf{r}) = -\frac{e\mathbf{F}(\mathbf{r})}{\hbar}, \tag{12}$$

where $\varphi(\mathbf{r})$ is the electrostatic potential. Then, we come back and express carrier energy as

$$E_n(\mathbf{k}) = \sum_{\beta=1}^{8} w_\beta E_{\beta n}(\mathbf{k}), \tag{13}$$

and carrier group velocity[15] as

$$v_{i,n}(\mathbf{k}) = \frac{ae}{2\pi\hbar}\sum_{\beta=1}^{8} w_\beta v_{i,\beta n}(\mathbf{k}), \tag{14}$$

where we take into consideration that the index β spans the eight vertices of a cube and w_β are the weights. Then, the weights[15] are given by

$$w_\beta = \left[1 - \frac{k_x - k_{x,\beta}}{\Delta}\right]\left[1 - \frac{k_y - k_{y,\beta}}{\Delta}\right]\left[1 - \frac{k_z - k_{z,\beta}}{\Delta}\right], \tag{15}$$

where $\Delta = 0.05 \times (2\pi/a)$. Finally, around each vertex we perform the linear interpolation for the carrier energy and velocity from the following,

$$E_{\beta n}(\mathbf{k}) = E_{\beta n} + \sum_{i=x,y,z}(k_i - k_{i\beta})\partial_i E_{\beta n}$$
$$+ \frac{1}{2}\sum_{i,j=x,y,z}(k_i - k_{i\beta})(k_j - k_{j\beta})\partial_{ij}^2 E_{\beta n}, \tag{16}$$

$$v_{i,\beta n}(\mathbf{k}) = \partial_i E_{\beta n} + \sum_{j=x,y,z}(k_j - k_{j\beta})\partial_{ij}^2 E_{\beta n}. \tag{17}$$

Next, for actual carrier scattering and in order to select the postcollision final state of the carrier, we need to use an inverse interpolation scheme as listed below. For this process, we note here that the first octant of the Brillouin zone is discretized as a course mesh of 108 cubes with a dimension $D_q = 4D_k = 0.2 \times (2\pi/a)$ and then for each of these a fine mesh of 512 cubes with a dimension $d_q = D_q/8 = 0.025 \times (2\pi/a)$.

C. Hot-carrier transport

With the Monte Carlo simulation and self-consistent Poisson solver,[19] we can examine how the hot electrons (holes) move in the bands; to do this we need to simultaneously solve the Boltzmann transport and Poisson equations. First, the Boltzmann transport equation is given by

$$\frac{\partial f(\mathbf{k},\mathbf{r},t)}{\partial t} = -\frac{d\mathbf{k}}{dt}\cdot\nabla_{\mathbf{k}}f(\mathbf{k},\mathbf{r},t) - \frac{d\mathbf{r}}{dt}\cdot\nabla_{\mathbf{r}}f(\mathbf{k},\mathbf{r},t)$$
$$+ \left(\frac{\partial f(\mathbf{k},\mathbf{r},t)}{\partial t}\right)_{\text{coll}}, \tag{18}$$

where $f(\mathbf{k},\mathbf{r},t)$ is the carrier distribution function at reciprocal space point $\mathbf{k}$ and real space point $\mathbf{r}$, while the collision term is given by

$$\left(\frac{\partial f(\mathbf{k},\mathbf{r},t)}{\partial t}\right)_{\text{coll}} = \sum_{\mathbf{k}'}\int\frac{d\mathbf{k}'}{(2\pi)^3}W(\mathbf{k},\mathbf{k}')f(\mathbf{k}')[1 - f(\mathbf{k})]$$
$$- \sum_{\mathbf{k}'}\int\frac{d\mathbf{k}'}{(2\pi)^3}W(\mathbf{k}',\mathbf{k})f(\mathbf{k})[1 - f(\mathbf{k}')], \tag{19}$$

where $W(\mathbf{k}',\mathbf{k})$ is the scattering rate for the transition given by $\mathbf{k} \to \mathbf{k}'$. Second, the Poisson equation is given by

$$\nabla\cdot[\varepsilon(\mathbf{r})\nabla\varphi(\mathbf{r},t)] = -\rho(\mathbf{r},t), \tag{20}$$

where $\varepsilon(\mathbf{r})$ is the static dielectric permittivity as a function of position and $\rho(\mathbf{r},t)$ is the free carrier charge density given by

$$\rho(\mathbf{r},t) = 2e\sum_{\text{(valence)}}\int\frac{d\mathbf{k}}{(2\pi)^3}f(\mathbf{k},\mathbf{r},t)$$
$$- 2e\sum_{\text{(conduction)}}\int\frac{d\mathbf{k}}{(2\pi)^3}f(\mathbf{k},\mathbf{r},t). \tag{21}$$

The Boltzmann transport and Poisson equations are coupled by the previous expressions for carrier free flight given by Eqs. (11) and (12).

D. DoS and photon absorption rate

In order to calculate the electronic DoS—crucial to the calculation of photon absorption as well as hot-carrier scattering processes—we use an algorithm originally developed in 1966 by Gilat and Raubenheimer (GR). This algorithm, involving discretization of the bands into tiny cubes, allows for the DoS to be determined for a given energy and location of a wave vector $\mathbf{k}$ by approximating the equivalent energy surfaces within the cubes by a set of parallel planes.[20] We will later use the notation $S_{(GR)}$ for the DoS calculated via the GR algorithm and $g(E)$ for the DoS at energy E.

Once we have calculated an accurate electronic DoS using the Gilat and Raubenheimer algorithm, we can then proceed to calculate the photon absorption rate. For this, we actually must consider the joint electronic DoS. This is shown in the following expression,[21] from Fermi's golden rule approximation (with the dipole approximation), for the photon absorption rate given by

$$I_{abs}(\hbar\omega) = \frac{\pi e^2}{m^2\varepsilon_\infty\omega}\sum_{v,c}\int\frac{d\mathbf{k}}{(2\pi)^3}|\mathbf{a}\cdot\langle\mathbf{k}_c|\hat{\mathbf{p}}|\mathbf{k}_v\rangle|^2$$
$$\times\delta(E_{\mathbf{k}}^c - E_{\mathbf{k}}^v - \hbar\omega), \tag{22}$$

where $\langle\mathbf{k}_c|$ and $|\mathbf{k}_v\rangle$ are the conduction and valence band Bloch states respectively, $\mathbf{a}$ is the polarization vector (whose effect
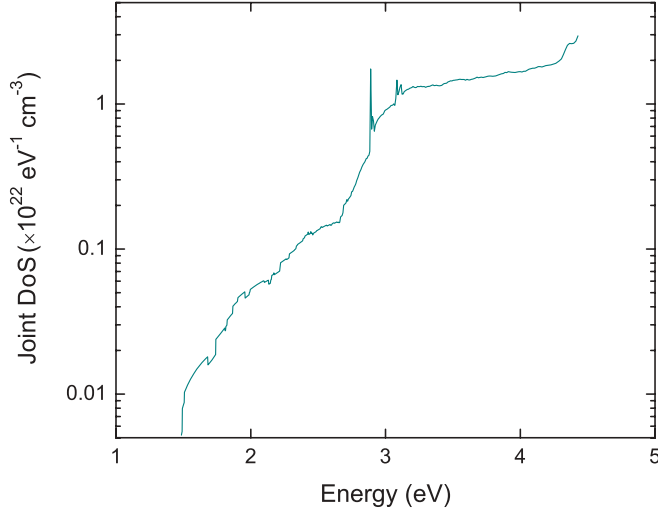
FIG. 3. (Color online) Calculated joint electronic DoS of GaAs. The cutoff at $\sim$4.43 eV ($\lambda = 280$ nm) corresponds to the ceiling of the AM1.5G reference solar spectrum.

is averaged to a value of $1/3$ for incoherent sunlight), $\mathbf{p}$ is the electron momentum, ω is the photon frequency, ε_∞ is the high-frequency permittivity, and the final term accounts for the joint electronic DoS. We show a plot of the calculated joint DoS in Fig. 3.

E. Short- and long-range Coulomb scattering

From Fermi's golden rule approximation (with the first Born approximation for a dilute electron gas), we can evaluate the short-range carrier-carrier scattering rate between a primary carrier and partner carrier[22] from

$$
\frac{1}{\tau_{ee}(\mathbf{k},\mathbf{r},n)} = \frac{2\pi}{\hbar} \sum_{\mathbf{k}',\mathbf{p}} \int \frac{d\mathbf{p}}{(2\pi)^3} f(\mathbf{p},\mathbf{r},m)
$$
$$
\times \int \frac{d\mathbf{k}'}{(2\pi)^3} |M_{ee}(\mathbf{k}'n',\mathbf{k}n;\mathbf{p}'m',\mathbf{p}m)|^2
$$
$$
\times \delta[E_n(\mathbf{k}) + E_m(\mathbf{p}) - E_{n'}(\mathbf{k}') - E_{m'}(\mathbf{p}')], \quad (23)
$$

where $\mathbf{k}(\mathbf{k}')$ represent the quasimomentum of the initial (final) state *primary* carrier (in band n) and $\mathbf{p}(\mathbf{p}')$ represent the quasimomentum of the initial (final) state *partner* carrier (in band m) with which a scattering collision occurred. The Coulomb matrix element, considering singlet and triplet states,[22] is given by

$$
|M_{ee}|^2 = \tfrac{1}{4}|M_d + M_x|^2 + \tfrac{3}{4}|M_d - M_x|^2
$$
$$
= |M_d|^2 + |M_x|^2 - \tfrac{1}{2}|M_d^* M_x + M_d M_x^*|, \quad (24)
$$

where the final *exchange* term is for the purpose of cross-section depression, when $\mathbf{k} - \mathbf{p} \ll \beta$, and M_d is the matrix element for the *direct* process

$$
M_d = \frac{e^2}{\varepsilon_s} \frac{\Im(\mathbf{k}'n',\mathbf{k}n)\Im(\mathbf{p}'m',\mathbf{p}m)}{|\mathbf{k} - \mathbf{k}' + \mathbf{G}|^2 + \beta^2(q_d,\omega_d)}, \quad (25)
$$

where $\Im$ are the overlap factors between the Bloch states given by

$$
\Im(\mathbf{k}'n',\mathbf{k}n) = \frac{1}{\Omega_c} \int_{\text{cell}} d\mathbf{r}\, u_{\mathbf{k}'n'}(\mathbf{r})^* u_{\mathbf{k}n}(\mathbf{r}) e^{i\mathbf{G}\cdot\mathbf{r}}, \quad (26)
$$

and $\beta(q,\omega)$ is the dynamic screening parameter given by $\beta(q,\omega) \approx q[\varepsilon(q,\omega)/\varepsilon_s - 1]^{1/2}$, with ε_s the static dielectric permittivity ($\sim$12.9 for GaAs). The dynamic screening parameter, $\beta(q,\omega)$, is evaluated at $q_d = |\mathbf{k} - \mathbf{k}' + \mathbf{G}|$ and at $q_x = |\mathbf{k} - \mathbf{p}' + \mathbf{G}|$. Meanwhile, M_x is the matrix element for the *exchange* process

$$
M_x = \frac{e^2}{\varepsilon_s} \frac{\Im(\mathbf{k}'n',\mathbf{p}m)\Im(\mathbf{p}'m',\mathbf{k}n)}{|\mathbf{k} - \mathbf{p}' + \mathbf{G}|^2 + \beta^2(q_x,\omega_x)}. \quad (27)
$$

From momentum conservation, we have $\mathbf{p}' = \mathbf{k} + \mathbf{p} - \mathbf{k}'$.

Now, within a Thomas-Fermi screening radius, a nearby partner carrier is selected[22] during the Monte Carlo simulation; this can be thought of as a statistical sampling of the carrier distribution, which is normalized to the carrier density as expressed by

$$
n(\mathbf{r}) = 2 \sum_m \int \frac{d\mathbf{p}}{(2\pi)^3} f(\mathbf{p},\mathbf{r},m). \quad (28)
$$

We then need to consider a fictitious self-scattering process in terms of a self-scattering rate expressed by

$$
\frac{1}{\tau_{ee}^{\text{self}}(\mathbf{k},\mathbf{r},n)} = \frac{\pi e^3 n(\mathbf{r})}{2\hbar \varepsilon_s^2 a^3} h(y_\pm,s) \sum_{\mathbf{G},\gamma} S_{(GR)} \left\{ \frac{1}{[|\mathbf{k} - \mathbf{k}_\gamma + \mathbf{G}|^2 + \beta(q_d,\omega_d)^2]^2} + \frac{1}{[|\mathbf{p} - \mathbf{k}_\gamma + \mathbf{G}|^2 + \beta(q_x,\omega_x)^2]^2} \right.
$$
$$
\left. - \eta \frac{1}{|\mathbf{k} - \mathbf{k}_\gamma + \mathbf{G}|^2 + \beta(q_d,\omega_d)^2} \frac{1}{|\mathbf{p} - \mathbf{k}_\gamma + \mathbf{G}|^2 + \beta(q_x,\omega_x)^2} \right\}, \quad (29)
$$

where $S_{(GR)}$ is the previously described electronic DoS calculated from the Gilat and Raubenheimer algorithm[20] and $h(y_\pm,s)$ is the phase-shift correction from Meyer and Bartoli.[23] The final term on the right-hand side of Eq. (29) is not included when electron-hole (distinguishable) collisions occur. The collision rate must be divided by two to prevent double counting as explained by Mošková and Moško.[24] The reasoning behind this self-scattering process protocol is so that we may either accept or reject a carrier-carrier collision with a

probability given by the overlap factor during the Monte Carlo simulation.

Long-range Coulomb interaction (electron-plasmon) is already accounted for in our Monte Carlo simulation routine; carriers are already coupled at long range, and the self-consistent nature of our Monte Carlo-Poisson solver step handles, at least in a semiclassical way, long-range carrier-carrier and carrier-plasmon scattering. The Poisson-solving step, therefore, is set to a frequency equal to or greater

TABLE I. Acoustic and optical deformation potentials for GaAs.

Conduction band acoustic intraband 1 (eV)	Conduction band acoustic interband and intrahigh bands (eV)	Conduction band optical intraband 1 (10^8 eV/cm)	Conduction band optical interband and intrahigh bands (10^8 eV/cm)	Valence band acoustic (eV)	Valence band optical (10^8 eV/cm)
5.0	3.5	2.1	1.5	6.3	11.3

than the electron gas plasma frequency denoted by

$$\omega_{\text{plasma}} = \sqrt{\frac{ne^2}{m_c \varepsilon_s}}, \tag{30}$$

where n is carrier density and m_c is the conductivity mass.

F. Electron-phonon scattering

Besides a scenario in which it is has been proposed that hot phonons (operating in the context of a phonon bottleneck effect) may help reheat the hot-electron gas, it is typically understood that electron-phonon scattering would not be fruitful for a HCSC due to the rampant onset of carrier relaxation. However, in order to simulate the effect of electron-phonon scattering (typically the polar longitudinal optical or LO phonons in GaAs at lower energies near the Γ valley and acoustic phonons at higher energies) on hot-carrier distribution, we include electron-phonon scattering[22] as part of our simulation. From Fermi's golden rule approximation (with the harmonic, adiabatic, and weak-coupling approximations), an expression for electron-phonon scattering rate is given by

$$\frac{1}{\tau_{ep}(\mathbf{k})} = \frac{2\pi}{\hbar} \sum_{\mathbf{q}} |M_{ep}(\mathbf{k}', \mathbf{k})|^2 \delta[E(\mathbf{k}) - E(\mathbf{k}') \mp \hbar\omega_{\mathbf{q}\eta}], \tag{31}$$

where the upper (lower) signs correspond to phonon emission (absorption). The *polar* phonon scattering Fröhlich matrix element[18] is

$$|M_{ep}(\mathbf{k}', \mathbf{k})|^2 = \frac{e^2 \hbar \omega_{LO}}{4q^2} \left(\frac{1}{\varepsilon_\infty} - \frac{1}{\varepsilon_s}\right) |\Im(\mathbf{k}', \mathbf{k})|^2$$
$$\times (n_{\text{phonon}} + 1/2 \pm 1/2), \tag{32}$$

and n_{phonon} is the phonon occupation number. The *nonpolar* scattering matrix element[18] (where ρ is the density of the semiconductor) is given by

$$|M_{ep}(\mathbf{k}', \mathbf{k})|^2 = \frac{\hbar}{2\rho\omega_{\mathbf{q}\eta}} \Delta_\eta^2 |\Im(\mathbf{k}', \mathbf{k})|^2 (n_{\text{phonon}} + 1/2 \pm 1/2). \tag{33}$$

We use the following approximations[15] for the electron-phonon matrix element given by

$$\Delta_\eta(\mathbf{k}', \mathbf{k}) = q \Delta_{ac}$$
$$\Delta_\eta(\mathbf{k}', \mathbf{k}) = (D_t K)_{op}, \tag{34}$$

and the following approximations[15] for acoustic phonon dispersion given by

$$\hbar\omega_{\mathbf{q}\eta} = \hbar\omega_{\eta,\max} [1 - \cos(qa/4)]^{1/2}; \quad (q < 2\pi/a)$$
$$\hbar\omega_{\mathbf{q}\eta} = \hbar\omega_{\eta,\max}; \quad (q \geqslant 2\pi/a), \tag{35}$$

where $\omega_{\eta,\max} = 4c_\eta/a$ and c_η is the velocity of sound with polarization η.

The acoustic and optical deformation potentials are shown in Table I.[18,25]

In our simulation, the electron-phonon scattering—taking into consideration the all-important electronic DoS again—is calculated from

$$\frac{1}{\tau_{ep}(\mathbf{k}, n)} = \frac{2\pi}{\hbar e a^3} \sum_{\beta n} |M_{ep}(\mathbf{k}', \mathbf{k})|^2 S_{(GR), \beta n}, \tag{36}$$

where we sum over cubes considering $E_{\beta n, \min} < E_n(\mathbf{k}) \pm \hbar\omega_{\mathbf{q}\beta n} \leqslant E_{\beta n, \max}$.

G. Impact ionization

As mentioned earlier, Würfel pointed out that impact ionization should be taken into consideration for hot-carrier redistribution in HCSC,[13] something that was not considered in the earlier analysis by Ross and Nozik.[2] Therefore, we include Monte Carlo simulation of impact ionization. We use the random-$\mathbf{k}$ approximation (i.e., ignoring momentum conservation and instead considering the importance of the joint DoS) as explained in 1967 by Kane,[26] which is valid for both electrons and holes in GaAs, and write down an expression for the scattering rate

$$\frac{1}{\tau_{ii}(E)} = \frac{2\pi}{\hbar} \frac{\Omega_c}{8} \langle M^2 \rangle \int_0^{E-E_g} dE_c \int_0^{E-E_g-E_c} dE_v g_c(E_c)$$
$$\times g_v(E_v) g_c(E - E_g - E_c - E_v), \tag{37}$$

where we assume that the Coulomb matrix element is constant or equivalent to its average value over all of the $\mathbf{k}$-points in the entire Brillouin zone as expressed by the following relationship,

$$\langle M^2 \rangle \approx \frac{e^4 a^4}{(2\pi)^4 \varepsilon_s^2} \kappa^2, \tag{38}$$

where κ is a number of order of 1. We then fit the impact ionization rate to a power-law sum

$$\frac{1}{\tau_{ii}(E)} = \sum_{r=1}^2 A_r (E - E_r)^{b_r}, \tag{39}$$

with fitting parameters provided in Table II.[25,27]

TABLE II. Impact ionization fitting parameters for GaAs.

	A_1 (s^{-1} eV^{-b})	E_1 (eV)	b_1	A_2 (s^{-1} eV^{-b})	E_2 (eV)	b_2
Electrons	1.95×10^8	1.51	3.0	2.64×10^{11}	1.80	6.5
Holes	3.41×10^{10}	1.51	3.0	2.80×10^{12}	1.90	4.5

VII. SIMULATION RESULTS AND DISCUSSION

It is our intent to consider a "best case" scenario. However, given the uncertainty regarding the exact implementation of HCSC, we consider two different cases. In both cases the solar cell is taken to be based on bulk GaAs, albeit only 100 nm thick and thus technically within the realm defined as "nanotechnology," under AM1.5G solar illumination at $1000 \times$ solar concentration. In Case 1 we consider the minimum possible density of thermal electrons outside the collection energy window of a selective contact (e.g., resonant tunneling diode or superlattice) by assuming that carriers optically generated and relaxing at energies outside the energy window will "somehow" be removed efficiently at the same rate (assumed to be a "generous" 10 ps) at which point hot-carriers will be removed by the ESC before relaxation. The opposite more realistic scenario in which thermalized carriers will be removed only via thermal recombination with a lifetime of 10 ns will be considered in Case 2 in order to assess the effect of Coulomb interparticle collisions in relaxing the photogenerated carriers at a realistically higher carrier density.

A. Case 1

For a GaAs (1.48 eV band gap at 0 K) HCSC with 100 nm thickness (for consideration of quasiballistic transport and hot-carrier extraction), substantial $1000 \times$ solar concentration, and artificially long (and, as stated before, overly generous) hot-carrier retention time (time before relaxation sets in) of 10 ps, we find after running our Monte Carlo simulation that carrier-carrier (Coulomb) scattering is not significant at the 1.85×10^{14} cm^{-3} carrier density, n_{hc}, involved here as determined[6] from

$$n_{hc} = \frac{\varphi_{hc} \tau_{hc} C}{d_{absorb}}, \tag{40}$$

where φ_{hc} is the AM1.5G photogenerated hot-carrier flux (1.85×10^{17} cm^{-2} s^{-1}, assuming one absorbed photon generates one electron-hole pair), τ_{hc} is the hot-carrier retention time (10 ps), d_{absorb} is the HCSC absorber layer thickness (100 nm), and C is the solar concentration ratio (1000). Similarly, upon running our Monte Carlo simulation, we find that impact ionization is ineffective. As mentioned earlier, we assume scattering due to ionized impurities to be negligible due to the intrinsic (undoped) nature of the hot-carrier absorber. Thus, the only relevant scattering mechanism is due to optical and acoustic phonons. Typically, interparticle Coulomb scattering and impact ionization scattering are not dominant processes below $\sim 10^{18}$ cm^{-3} carrier density. Therefore, even if carrier retention time was increased to 100 ps and solar concentration

increased to $10\,000 \times$, then the carrier density would only increase to 10^{16} cm^{-3}.

The aforementioned carrier retention time may be thought of as the *effective* carrier lifetime in the special case of the HCSC as the traditional concept of a minority-carrier lifetime (i.e., minority charge carriers operating under a fully relaxed diffusive transport regime) does not apply here. Historically, it has often been quoted in the literature that the minority electron lifetime for GaAs is of the order of 1–10 ns.[28,29] For high-quality epitaxially grown GaAs (minimal bulk defects) with wide band-gap lattice-matched Al$_x$Ga$_{1-x}$As or Ga$_{0.52}$In$_{0.48}$P passivation layers (for minimal surface recombination), it is assumed that radiative recombination drives the minority-carrier lifetime. However, by the time 1–10 ns has passed, the charge carriers have long since fully relaxed to their respective fundamental band edges due to the inevitable interaction with lattice phonons (as shown later in Fig. 7), and absent of nonradiative recombination, they are then prone to band-to-band (i.e., radiative) recombination. For successful operation of a HCSC, the charge carriers would clearly have to be extracted through their respective ESC before both relaxation and radiative recombination occur; otherwise, the endeavor to achieve a higher voltage through selective extraction of the hot, higher energy carriers would be a failure.

Recycled photons (due to light trapping) can radiatively recombine resulting in approximate band-gap energy luminescence, which upon reabsorption leads to approximate band-gap energy electron-hole pairs. However, these carriers are not hot and thus are not useful for a HCSC (i.e., the near-band-edge carriers will have energy less than the ESC). Moreover, these approximate band-gap energy carriers cannot be effectively extracted out as useful photocurrent as they will be impeded by the barrier layers that comprise the selective contact structures shown in Fig. 1.

As a cross check, we also consider the role of Auger recombination and compare it to radiative recombination in the GaAs HCSC absorber. The Auger recombination coefficient (A)[30] for GaAs is 7×10^{-30} cm^6 s^{-1} and the radiative recombination coefficient (B)[29] is 7×10^{-10} cm^3 s^{-1}. It is also known that Auger recombination can become an issue at high carrier concentration (or doping concentration, but we have already assumed that our HCSC absorber is undoped), so instead of the $\sim 10^{14}$ cm^{-3} carrier density discussed earlier, we will now examine the more severe case in which the photogenerated carrier density is equal to 1.85×10^{17} cm^{-3} (corresponding to a 10 ns "lifetime" and $1000 \times$ solar concentration). The Auger recombination rate is given by An^2, and the radiative recombination rate is given by Bn, where n is the carrier concentration. Even for this severe case and certainly for that of the 10^{14} cm^{-3} carrier density, radiative recombination dominates Auger recombination, and so we find that Auger recombination (the reciprocal process of impact ionization) is an ineffective mechanism in so far as supporting HCSC operation in GaAs.

With all of this in mind, the hot-carrier distribution upon photogeneration is now illustrated as a histogram in Fig. 4. Most notably, the distribution is wide, as to be expected, on account of the polychromatic solar spectrum.
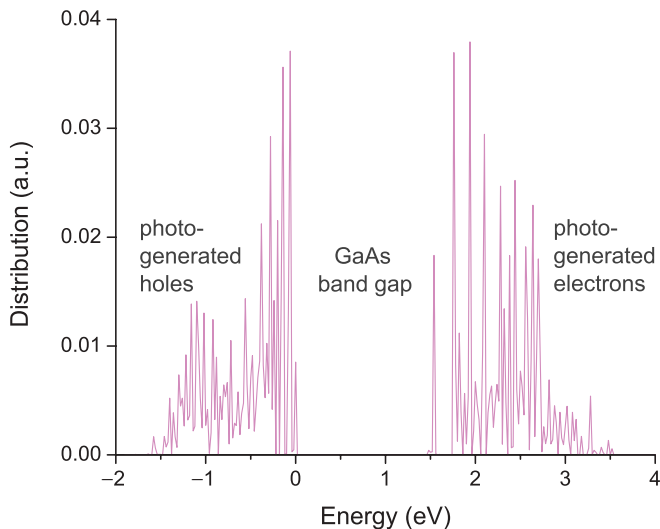
FIG. 4. (Color online) Histogram of hot electron (hole) energy distribution upon photogeneration in GaAs. The wide distribution is a natural artifact of the polychromatic AM1.5G solar spectrum and the available joint electronic DoS (in GaAs). The challenge of extracting all of the widely distributed hot electrons (holes) through narrow ESC windows is daunting.

1. Current density

From the photogenerated charge carrier distribution shown in Fig. 4, we observe a peak hot-electron distribution at 1.94 eV, suggesting this is where hot electrons are (at least locally) concentrated immediately upon photogeneration. We then calculate the photogenerated current density for a HCSC (1 cm^2 active area and 100 nm thick with a resonant tunneling ESC for electrons on the topside and separately for holes on the rear side) in which the hot-electron ESC is centered at 1.94 eV and the width of the contact (in units of electron volts) has been artificially relaxed to be $\sim k_B T$ in violation of Eq. (1). With the ESC centered at 1.94 eV (639 nm), we make the current density calculation by integrating (via the trapezoidal rule) the AM1.5G spectral photon flux shown in Fig. 5 over
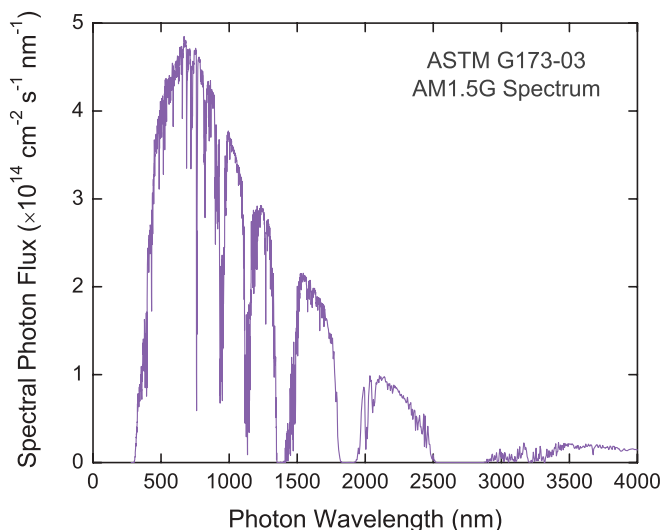
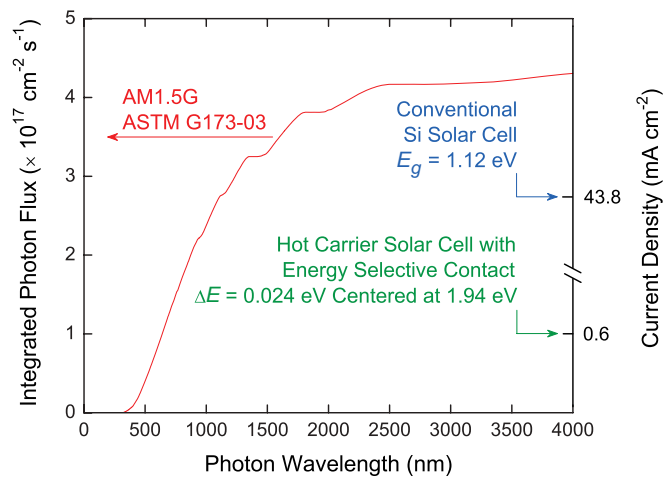

FIG. 5. (Color online) AM1.5G spectral photon flux.

FIG. 6. (Color online) Photogenerated current density for a HCSC, where all hot electrons can only be collected by an ESC centered at 1.94 eV with $\Delta E \approx 0.024$ eV versus a standard Si solar cell that is able to collect relaxed electrons. This current density (one sun) is calculated from the AM1.5G spectrum.

the photon wavelengths (energy) of relevance, approximately 635–643 nm, which corresponds to $\Delta E \approx 0.024$ eV, and then we multiply this by the electronic charge (1.602 $\times$ 10^{-19} C) so that we can determine the photogenerated current density available at our hot-electron ESC as shown in Fig. 6.

From this, we can then quantify the actual current that could be collected by our resonant tunneling diode ESC as a function of ΔE. As may be seen from Fig. 6, the photogenerated current density produced by a HCSC with ΔE centered at 1.94 eV and relaxed to be as large as $\sim k_B T$, and thus already in violation of Eq. (1), is not only trivial at ~ 0.6 mA cm^{-2} (one-sun current density), but it is also almost two orders of magnitude less than that from a standard Si solar cell. We show a Si solar cell here as a generic example of a common solar cell technology. For context, the maximum AM1.5G 1 $\times$ current density for a 1.48 eV band gap ($E_{g,\text{GaAs}}$ at 0 K) solar cell is 29.7 mA cm^{-2}.

2. Carrier relaxation

Subsequent carrier relaxation is shown in Fig. 7. During the relaxation process, some of the higher-energy hot electrons linger in the X and L satellite valleys of GaAs. However, at no instance do all hot electrons redistribute into a narrow energy window required for successful hot extraction. Furthermore, the onset of relaxation in essence undermines the core concept of the HCSC, where the goal is to extract carriers prior to any interaction with lattice phonons.

B. Case 2

Previously, we assumed that all photogenerated carriers are removed within a "retention time" of 10 ps for a steady-state density (under solar optical generation and carrier recombination or removal) of about 1.85 $\times$ 10^{14} cm^{-3}. We found that relaxation of the hot photogenerated carriers occurs on a time scale of ~ 1 ps. So, the density of carriers in the "active" region (i.e., collection energy window) is expected to correspond to the density of hot carriers we would have if the
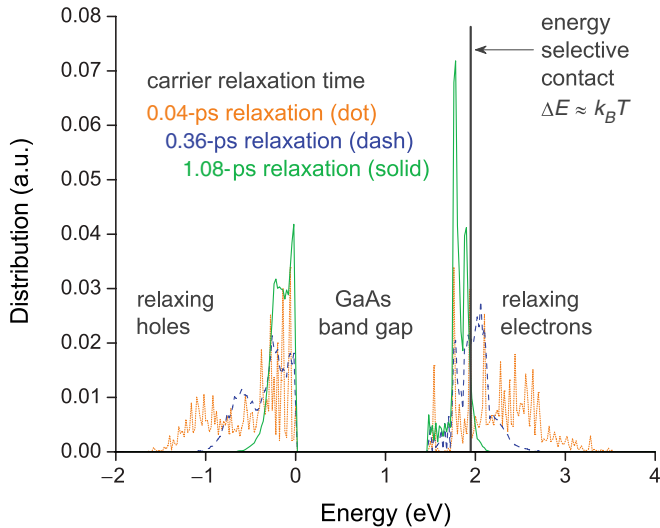
FIG. 7. (Color online) Histogram of hot electron (hole) energy distribution upon relaxation in GaAs. Relaxation results from the rapid onset of carrier-phonon interaction. An example ESC for electrons centered at 1.94 eV is shown where the width of the vertical line approximately corresponds to an energy selectivity of $\Delta E = k_B T_{300K} \approx 0.026$ eV.

total density were a factor of 10 smaller. This resulted in an available current density of $\sim$0.6 mA cm^{-2}.

Now, we consider the more realistic scenario in which carriers within the collection energy window are collected in this short time, but the *remaining* carriers survive for a much longer thermal recombination lifetime of 10 ns. This constitutes a more realistic scenario in which interparticle collisions at this higher density may alter the dynamics of the relaxation process.

Let us consider again a 100-nm-thick GaAs absorber. As in the simulation discussed previously, we assume an incoming flux of 1.85×10^{17} photons cm^{-2} s^{-1} and now a carrier *recombination lifetime* of 10 ns. We have also made the "optimal" choice of a collection energy window centered at 1.94 eV.

Before presenting the details of the simulation and the results, let us discuss our expectations. Roughly speaking, at steady state there will be a carrier density of about 1.85×10^{17} cm^{-3}, which will have already had ample time to *thermalize* to energies of the order $k_B T$. Meanwhile, there will be 1.85×10^{14} "hot" electrons cm^{-3} generated by the absorbed sunlight. So, if our estimate of the "retention time" (10 ps) is correct, 99.9% of the carriers will be thermal, while only 0.1% of the total will be due to the "hot" optically generated carriers. While one may expect that the large density (99.9% of the total density) of thermal electrons may help to repopulate the electron energy distribution at energies of 1.94 eV via interparticle Coulomb collisions, this is extremely unlikely, and actually a much more negative result may be expected for the following reasons.

First, for interactions involving particles with significantly different energies, statistical arguments based on the joint DoS of the recoil particles (equipartition) strongly suggest that the hot carriers will be removed from the high-energy region by

losing a large fraction of their energy. So, the high-density thermal carriers will not be able to simply "nudge" the hot-carrier distribution and repopulate the collection energy window but instead will predominantly absorb a large fraction of the hot-electron energy and speed up the hot-electron relaxation process, entirely removing hot carriers from the "useful" energy region. Another way to see this is to note that at steady state, the average electron energy will be almost thermal. Interparticle collisions—as seen from detailed balance considerations—will drive the distribution toward equilibrium, thus washing out the hot distribution of optically generated carriers at a rate even faster than carrier-phonon interactions. Better results would be obtained only at a much higher optical generation rate, possibly at unrealistically high concentrations of sunlight of the order of 10^5 to 10^6 (compared to the maximum possible concentration of $\sim$4.6 $\times$ 10^4),[9] resulting in a steady-state density of hot electrons comparable to the density of the thermalized carriers.

Second, in a simple parabolic-band approximation, the unscreened scattering rate for Coulomb particle-particle collisions may be calculated analytically in the center-of-mass frame and can be shown to scale with the inverse of the relative (crystal) momentum Δq, so the probability of exchanging energy between a thermal particle of energy $E \sim k_B T$ and a hot particle of energy $E \gg k_B T$ decreases with increasing E as $(k_B T/E)^{1/2}$. (This may be understood physically by adopting a reference frame in which one particle is at rest so that the scattering between particles of significantly different energies will appear as scattering of a high-energy particle with a static Coulomb potential. In this case, the high-energy "incident" particle will see a "weaker" scattering potential compared to its kinetic energy and—similar to what is well known in the case of impurity scattering—the rate will decrease with the inverse square root of the initial energy, the "relative energy" in our case.) So, even at small densities, collisions between thermal and hot-carriers cannot contribute efficiently to a "repopulation" of the hot-electron distribution around the collection energy window. Admittedly, dielectric screening reverses this trend: At large densities ($>10^{19}$ cm^{-3} or so), the denominator of the interparticle Coulomb matrix element is dominated by the screening parameter and dynamic screening (which, in any event, is accounted for in our simulations) actually favors processes involving a large momentum and energy transfer (as we have studied in the past). But the densities of interest here are much smaller than this unless, as we said earlier, we consider the unrealistic concentration of sunlight. This is in direct contrast with interactions between the hot electrons themselves: In this case, interactions are more frequent, and equipartition suggests an effective repopulation of the collection energy window.

It follows that it will be "predominantly" those 1.85×10^{14} electrons cm^{-3} (ignoring holes, which however have been included in our simulations), which will be able to repopulate the energy window, while the much more numerous thermal electrons will either have little or no effect (at low densities) or may even speed up the relaxation process (at higher densities).

In this new simulation, we assume as an initial condition that 1.85×10^{17} carriers cm^{-3} have been optically generated and allowed to relax. This enables us to study the details of the relaxation dynamics. Simultaneously, carriers "hitting" the
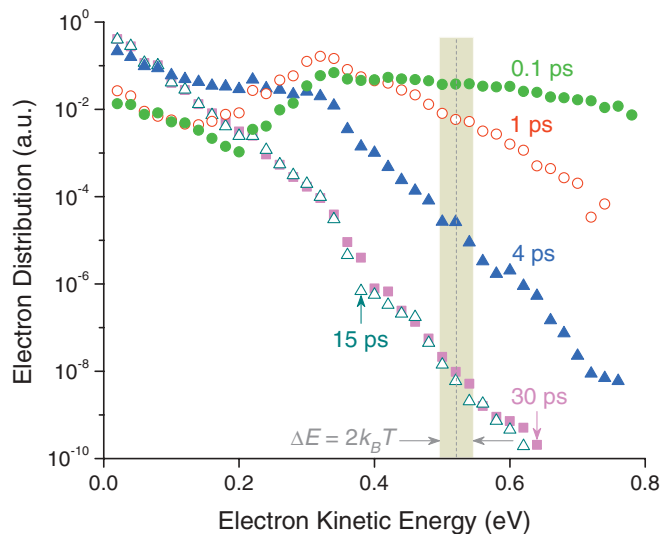
FIG. 8. (Color online) Distribution of electrons from transient to steady state. Steady state is reached at ∼15 ps. The conduction-band minimum has been set equal to zero here. The ESC centered at 1.94 eV is now referenced to the bottom of the conduction band, so at ∼0.52 eV and has been widened to $2k_BT$.
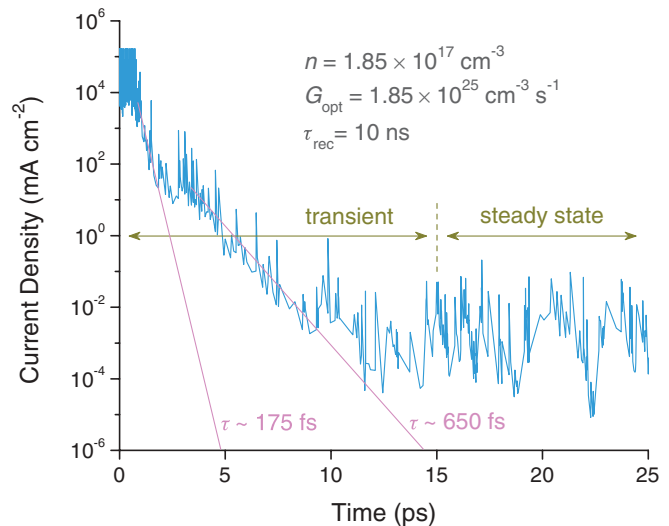

FIG. 9. (Color online) Decay of the available current density (AM1.5G one-sun equivalent) in the energy window centered at 1.94 eV with width $2k_BT$. The data are calculated from Monte Carlo simulations. Note a plateau at ∼2 to 3 ps due to carriers decaying quickly to satellite valleys before transferring slowly to the Γ valley. Thus, two exponential time constants are shown: a decay constant of ∼175 fs associated with relaxation in the satellite valleys and a decay constant of ∼650 fs associated with relaxation due to intervalley scattering. The fluctuation in the data is associated with the frequency at which simulated particles are generated optically.

"bottom" interface with energy in the collection window were removed and tagged as "collected current" with carriers also being continuously generated optically at a rate of 1.85×10^{20} pairs cm^{-2} s^{-1} (i.e., 1.85×10^{25} pairs cm^{-3} s^{-1} integrated over the 100 nm thickness of our HCSC absorber), thus mimicking steady-state conditions under concentration of $1000 \times$ sunlight. Thermal recombination can be ignored because this is indeed a process too slow in our picosecond time scale to play any role besides setting the value of the density at steady state. As anticipated, the electron distribution at energy $>k_BT$ is relaxed much more effectively than in the low-density case we had assumed before, and our estimate of the current density drops from 0.6 mA cm^{-2} to ∼2×10^{-3} mA cm^{-2}, mainly caused by the extremely short time (∼175 fs) at which hot carriers are removed from the collection energy window. Although in violation of Eq. (1), we have increased the width of the ESC window from k_BT (Case 1) to $2k_BT$ (Case 2) in order to model an even more conservative scenario; in this context the time evolution of the electron distribution is shown in Fig. 8. The rapid "washing out" of the hot-carrier component is now caused not only by inelastic electron-phonon collisions but also by the efficient relaxation of the hot carriers due to interparticle collisions with the thermal component. Meanwhile, the decay of the collected current is illustrated in Fig. 9, where a large "transient" current density is seen initially because of the large density of carriers we have assumed and the fact that the initial carrier energy distribution is due uniquely to the solar-optical generation. Already within ∼2 to 3 ps, the density of electrons at the collection energy drops with a "relaxation" time constant of about 175 fs (due to scattering within the satellite valleys). Following this, the exponential decay "relaxation" time constant is about 650 fs (due to intervalley scattering). At ∼15 ps, steady state is reached, and the current density saturates at a value of a few microamperes per centimeter squared.

C. Multiple junctions

Referring to Fig. 5, we can see that the AM1.5G spectrum is photon dense between 1.42 eV (873 nm) and 1.94 eV (639 nm). Thus, even if the ESC is placed at ∼1.94 eV and even if those higher energy electrons that have relaxed down to 1.94 eV can be extracted, roughly 50% of the electrons would be lost because the spectral photon flux is evenly split between 1.42–1.94 eV and 1.94–4.43 eV (AM1.5G ceiling). In other words, there does not appear to be any viable mechanism to redistribute the lower energy electrons (ranging from 1.42 to 1.94 eV) to a fixed ESC level at 1.94 eV. However, we can take inherent advantage of this spectral photon flux distribution as discussed next and thus avoid the pitfalls of the HCSC.

The natural way to overcome the inherent limitations of the HCSC concept is to employ vertically stacked multiple junctions[31,32] with subcell band-gap energy increasing from bottom to top, and with the subcells connected in series with tunnel diodes,[33] as shown in Fig. 10, so that their output voltage is additive.

By considering the absorption coefficient and base layer thickness (and more precisely also the quantum efficiency and any reflective loss), each subcell can be designed to achieve matched photogenerated current density. For example, under the AM1.5G spectrum, a 1.42-eV GaAs solar cell can have photogenerated current density up to ∼32 mA cm^{-2}. If a lattice matched 1.94-eV AlGaInP p–n junction subcell is added on top of the GaAs cell, then each subcell can produce ∼16 mA cm^{-2}. Ultimately, this 1.94/1.42 eV double junction solar cell can generate more power from the higher-energy photons that would normally experience significant relaxation loss in a 1.42-eV GaAs solar cell alone. We stress here that the
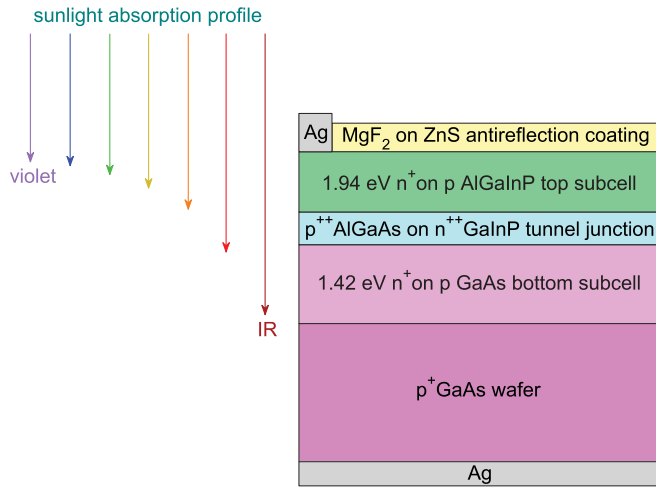
FIG. 10. (Color online) Series-connected, two-terminal, current-matched monolithic double-junction solar cell with 1.94-eV top and 1.42-eV bottom subcells. A high-efficiency double-junction solar cell can take the place of a HCSC by minimizing total relaxation loss in a practical architecture.

FIG. 11. (Color online) Schematic representation (in **k**-space) of momentum randomization (considering only the arbitrarily chosen x direction here) of a photogenerated hot electron. If the hot electron does not have momentum (velocity vector, $\mathbf{v}_{+x}$) directing it to the ESC for extraction at the macroscopic metal electrodes, then the chances of it being collected diminishes.

double junction cell achieves the goal of lower total relaxation loss but does so in a realizable architecture that may be tuned to match the incident solar spectrum (the binning of photon flux) in which standard solar cell physics applies (including detailed balance), carriers are expected to relax in their respective p–n junction subcells, conventional minority-carrier lifetimes apply, and drift-diffusion explains the charge carrier transport behavior.

D. Power conversion efficiency

The detailed balance-limiting[34,35] theoretical power conversion efficiency (AM1.5G spectrum; $P_{in} = 0.1 \, \mathrm{W \, cm^{-2}}$; 298 K) for the aforementioned 1.94/1.42 eV double-junction solar cell is 40.4% ($V_{max} \approx 2.58$ V and $J_{max} \approx 15.64 \, \mathrm{mA \, cm^{-2}}$). In comparison, the power conversion efficiency for a HCSC producing 1.94 V and 0.6 mA cm^{-2} (see Fig. 6) is only 1.16%. As a benchmark, a 1.42-eV GaAs single-junction solar cell has a detailed balance-limiting power conversion efficiency of 33.2% under the aforementioned conditions. While the voltage of a HCSC can be set arbitrarily (within reason) by the placement of the ESC, the severely reduced current density imposed by the failure to extract a sufficient amount of the widely distributed photogenerated charge carriers appears to be the limiting bottleneck in terms of HCSC performance and power conversion efficiency. This is in direct contrast to the design of conventional solar cells in which it is relatively easy to achieve nearly peak current density but much more challenging to converge on the peak (detailed balance-limiting) voltage. We note here that the HCSC current density, although already trivial, is likely too large. We find from our Monte Carlo simulation that upon photogeneration, there is a 50% probability that the momentum of the hot electrons will be directed away from the electron ESC. In other words, the hot electrons that need to travel quasiballistically (say, in the positive x direction) to the ESC for extraction will actually have a velocity vector component (opposite, negative
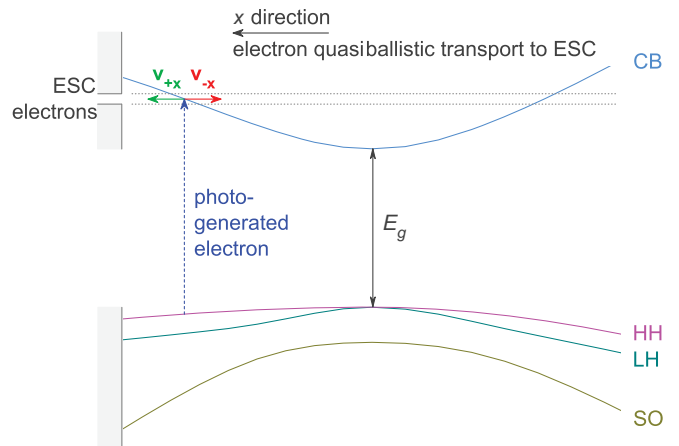
x direction) that would prevent them from heading in the correct direction as shown schematically in Fig. 11.

In conventional solar cells, momentum randomization is not an issue because the relaxed charge carriers have time to diffuse to the contact electrodes, and thus the precise nature of their velocity vectors is not critical. However, in the HCSC, time is critical, and thus tremendous demands are placed on both hot-carrier transport and selective extraction.

VIII. CONCLUSION

We have investigated in detail the feasibility of operation of HCSC. Within the context of a realistic full band structure and actual broadband AM1.5G solar spectrum, we have modeled the wide distribution of photogenerated charge carriers and then the subsequent carrier-phonon scattering (relaxation) processes in GaAs—a zinc-blende semiconductor that has similar electronic DoS with other common semiconductors used for solar cells (and thus this condition coupled with the polychromatic nature of the solar spectrum naturally leads to widely dispersed photogenerated hot carriers in the bands independent of choice of common solar cell semiconductors). We find both quantitatively and qualitatively that it is unrealistic to expect to take the widely distributed ensemble of photogenerated hot electrons and rapidly redistribute them to a singular (or even near singular) energy level, while simultaneously ensuring that they have the proper momentum vector that would allow them to directly transport in a quasiballistic fashion precisely to the selective energy level of the resonant tunneling ESC. The chance of this happening consistently in field-deployed mass production solar cells, GaAs or otherwise, would be improbable.

Furthermore, if we could somehow forgo the disorder induced by scattering and thus direct the hot electrons with a relatively narrow-angle cone of transport, we see, nonetheless, that the slightest perturbation off of resonance at the ESC severely degrades the peak tunneling current and, moreover,

any minor deviation from Eq. (1) in terms of ΔE relaxation breaks the goal of isentropic hot-electron cooling and thus breaks down the original concept of the HCSC to begin with.

Notably, HCSC physics is different than conventional relaxed carrier solar cell physics. As a result, it appears that we may need to "recalibrate" our mentality of what constitutes carrier lifetime. The time span that photogenerated carriers are hot (i.e., their "retention" time before relaxation) replaces conventional minority-carrier lifetime. Also, selective contact structures for isentropic extraction are required, and we must be aware that the photogenerated hot carriers remain widely distributed as they momentarily equilibrate at a temperature greater than that of the lattice. Additionally, in order to avoid interaction with phonons, we may have to rely on quasiballistic transport rather than conventional diffusive charge carrier transport, and thus the issue of carrier momentum should not be forgotten.

Finally, considering what has been discussed so far, is there then a viable pathway forward for the realization of a HCSC with power conversion efficiency exceeding an optimized single-junction solar cell? Although there appear to be some challenges, we leave open the possibility of eventual realization of a HCSC that has greater efficiency than the best single-junction solar cells. In the context of conceptually modeling an optically induced impact ionization solar cell, Werner, Kolodinski, and Queisser pointed out that an inverse band structure[36] design approach may be important, and perhaps this too would apply toward the design of a successful (i.e., high efficiency) HCSC. Meanwhile, the race for continued enhancement in solar cell efficiency is well underway in an already known and field-tested approach that bypasses the design constraints and challenges with HCSC. This approach involves the use of monolithic, series-connected multiple junctions, whereby photogenerated carriers are collected in subcells that have band-gap energy closer to the absorbed photon energy for a reduction in total relaxation loss, while providing a way to realize increased voltage, improved areal power density, and increased power conversion efficiency.

ACKNOWLEDGMENT

---

*apkirk@utdallas.edu

†max.fischetti@utdallas.edu

[1] http://www.astm.org/Standards/G173.htm, (June 17, 2012).

[2] R. T. Ross and A. J. Nozik, J. Appl. Phys. **53**, 3813 (1982).

[3] H. Fröhlich, Proc. R. Soc. London Ser. A **188**, 521 (1947).

[4] R. Clady, M. J. Y. Tayebjee, P. Aliberti, D. König, N. J. Ekins-Daukes, G. J. Conibeer, T. W. Schmidt, and M. A. Green, Prog. Photovoltaics **20**, 82 (2012).

[5] S. M. Goodnick, S. Limpert, C. Honsberg, and P. Lugli, in *38th IEEE Photovoltaic Specialists Conference* (IEEE Conference Publications, Austin, 2012), p. 1657.

[6] Y. Takeda, T. Ito, T. Motohiro, D. König, S. Shrestha, and G. Conibeer, J. Appl. Phys. **105**, 074905 (2009).

[7] D. König, K. Casalenuovo, Y. Takeda, G. Conibeer, J. F. Guillemoles, R. Patterson, L. M. Huang, and M. A. Green, Phys. E (Amsterdam) **42**, 2862 (2010).

[8] D. K. Ferry and S. M. Goodnick, *Transport in Nanostructures* (Cambridge University Press, Cambridge, 1997).

[9] P. Würfel, *Physics of Solar Cells: From Basic Principles to Advanced Concepts*, 2nd ed. (Wiley-VCH, Weinheim, 2009).

[10] C. Kittel, *Elementary Statistical Physics* (Wiley, New York, 1958).

[11] R. G. Chambers, Proc. Phys. Soc. London **65**, 458 (1952).

[12] H. F. Budd, J. Phys. Soc. Jpn. **18**, 142 (1963).

[13] P. Würfel, Sol. Energy Mater. Sol. Cells **46**, 43 (1997).

[14] T. Kurosawa, J. Phys. Soc. Jpn. Suppl. **21**, 424 (1966).

[15] M. V. Fischetti and S. E. Laux, Phys. Rev. B **38**, 9721 (1988).

[16] H. Shichijo and K. Hess, Phys. Rev. B **23**, 4197 (1981).

[17] J. R. Chelikowsky and M. L. Cohen, Phys. Rev. B **14**, 556 (1976).

[18] M. V. Fischetti, IEEE Trans. Electron Devices **38**, 634 (1991).

[19] S. E. Laux and M. V. Fischetti, in *Numerical Aspects and Implementation of the DAMOCLES Monte Carlo Device Simulation Program, in Monte Carlo Device Simulation: Full Band and Beyond*, edited by K. Hess. (Kluwer Academic, Norwell, MA, 1991), p. 123–160.

[20] G. Gilat and L. J. Raubenheimer, Phys. Rev. **144**, 390 (1966).

[21] K. Hess, *Advanced Theory of Semiconductor Devices* (Wiley-IEEE Press, New York, 2000).

[22] M. V. Fischetti, S. E. Laux, and E. Crabbé, J. Appl. Phys. **78**, 1058 (1995).

[23] J. R. Meyer and F. J. Bartoli, Phys. Rev. B **23**, 5413 (1981).

[24] A. Mošková and M. Moško, Phys. Rev. B **49**, 7443 (1994).

[25] http://www.research.ibm.com/DAMOCLES/html_files/numerics.html (June 17, 2012).

[26] E. O. Kane, Phys. Rev. **159**, 624 (1967).

[27] N. Sano, M. V. Fischetti, and S. E. Laux, in *Extended Abstracts of 1998 Sixth International Workshop on Computational Electronics*, (IEEE Conference Publications, New York, 1998), pp. 198–201.

[28] S. M. Sze, *Physics of Semiconductors*, 2nd ed. (John-Wiley & Sons, New York, 1981).

[29] M. Levinstein, S. Rumyantsev, and M. Shur, *Handbook Series on Semiconductor Parameters Volume 1: Si, Ge, C (Diamond), GaAs, GaP, GaSb, InAs, InP, InSb* (World Scientific, Singapore, 1996).

[30] O. D. Miller, E. Yablonovitch, and S. R. Kurtz, IEEE J. Photovoltaics **2**, 303 (2012).

[31] E. D. Jackson, in *Transactions of the Conference on the Use of Solar Energy—The Scientific Basis* (University of Arizona Press, Tucson, 1955), p. 122.

[32] E. D. Jackson, US Patent No. 2,949,498 (August 16, 1960).

[33] L. Esaki, Phys. Rev. **109**, 603 (1958).

[34] W. Shockley and H. J. Queisser, J. Appl. Phys. **32**, 510 (1961).

[35] C. H. Henry, J. Appl. Phys. **51**, 4494 (1980).

[36] J. H. Werner, S. Kolodinski, and H. J. Queisser, Phys. Rev. Lett. **72**, 3851 (1994).